Sea Ice Change Detection in SAR Images Based on Convolutional-Wavelet Neural Networks

Feng Gao, Xiao Wang, Yunhao Gao, Junyu Dong, and Shengke Wang

***Abstract*— Sea ice change detection from synthetic aperture radar (SAR) images can be regarded as a classification procedure, in which pixels are classified into changed and unchanged classes. However, existing methods usually suffer from the intrinsic speckle noise of multitemporal SAR images. To solve the problem, this letter presents a change detection method based on convolutional-wavelet neural networks (CWNNs). In CWNN, dual-tree complex wavelet transform is introduced into convolutional neural networks for changed and unchanged pixels' classification, and then, the effect of speckle noise is effectively reduced. In addition, a virtual sample generation scheme is employed to create samples for CWNN training, and the problem of limited samples is alleviated. Experimental results on two real SAR image data sets demonstrate the effectiveness and robustness of the proposed method.**

***Index Terms*— Change detection, convolutional-wavelet neural network (CWNN), sea ice, synthetic aperture radar (SAR) images.**

I. Introduction

THERE have been growing interests in the Arctic and Antarctic sea ice monitoring, since changes of sea ice are important for navigation safety and natural resource extraction. Many ships and fishing vessels are not ice-strengthened and must therefore avoid all ice areas. Especially, when the ice pressure is high, even the most powerful icebreakers can hardly move forward through the ice pack. In order to support safe navigation, changed information of the ice coverage is of significant value. In this letter, we focus on sea ice change detection, which is defined as identifying significantly changed areas in sea ice by analyzing two remote sensing images captured over the same geographical area.

Synthetic aperture radar (SAR) images are acquired by active microwave sensors and are widely used in the sea ice monitoring. SAR sensors have been proved to be the ideal source for sea ice monitoring, because they can monitor sea ice independently of sunlight conditions and cloud coverage. However, due to the lack of robust automatic image interpretation techniques, SAR images are still manually interpreted for ice by national ice agencies [1]. SAR images' interpretations are time-consuming and subjective. In addition, SAR image change detection is challenging due to the presence of the intrinsic multiplicative speckle noise [2]. Therefore, it is essential to develop a robust sea ice change detection technique against the speckle noise.

There has been a long-term effort toward automatic change detection from SAR images. The most popular techniques include thresholding and clustering [3]. Bazi *et al.* [4] used the Kittler and Illingworth minimum-error thresholding algorithm for SAR image change detection. In [5], a change detection method based on a genetic expectation–maximization thresholding algorithm was proposed. At the same time, clustering-based methods were proposed for SAR image change detection. In [6], the change detection is achieved by partition pixels into two groups by using k-means clustering. Gong *et al.* [7] proposed a change detection method based on reformulated fuzzy local-information c-means clustering. The spatial context is integrated in a fuzzy way for the purpose of reducing the effect of speckle noise. Besides the above-mentioned techniques, some studies focus on feature extraction from remote sensing images. Li *et al.* [8] used Gabor wavelet representations to exploit the changed information. Wang *et al.* [9] presented a remote sensing image analysis method based on a locality adaptive discriminant analysis, which can adaptively exploit the local manifold structure of data.

High-level image representations need to be used in order to capture ice appearances from multitemporal SAR images. Handcrafting such features is rather difficult. Recently, deep learning methods have achieved an excellent performance in image classification [10]–[13]. These methods can learn the representative and discriminative features in a hierarchical manner from the original data [14] and the promising results have been reported. Wang *et al.* [13] presented a general end-to-end 2-D convolutional neural network (CNN) framework for change detection. In [1], it is suggested that CNN could provide deep representations for sea ice concentration estimation in SAR images. Duan *et al.* [15] presented an SAR image segmentation method based on convolutional-wavelet neural networks (CWNNs), in which a wavelet constrained pooling layer is designed to replace the conventional pooling in CNN. The wavelet constrained pooling layer can suppress the speckle noise and therefore provides a better performance in an SAR image analysis.

In this letter, we investigate the application of CWNN in the sea ice change detection. First, an initial change map

Manuscript received September 10, 2018; revised December 26, 2018; accepted January 22, 2019. Date of publication February 13, 2019; date of current version July 18, 2019. This work was supported in part by the National Natural Science Foundation of China under Grant 41606198, Grant 41576011, and Grant U1706218, and in part by the Natural Science Foundation of Shandong Province under Grant ZR2016FB02. *(Corresponding author: Junyu Dong.)*

The authors are with the Qingdao Key Laboratory of Mixed Reality and Virtual Ocean, School of Information Science and Engineering, Ocean University of China, Qingdao 266100, China (e-mail: dongjunyu@ouc.edu.cn).

Color versions of one or more of the figures in this letter are available online at http://ieeexplore.ieee.org.

Digital Object Identifier 10.1109/LGRS.2019.2895656

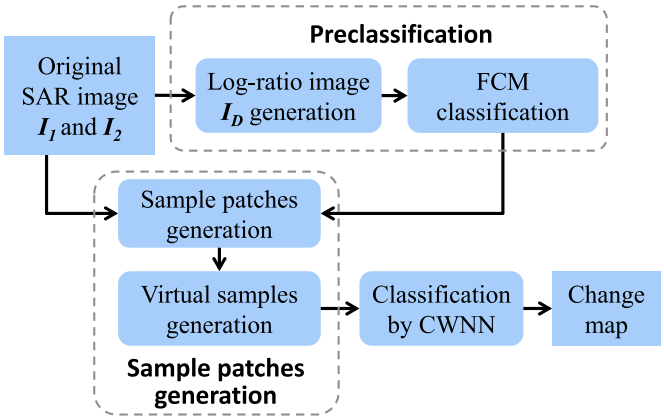

Fig. 1. Illustration of the proposed framework.

is generated by a clustering algorithm. Second, samples are selected from the initial change map and fed into CWNN for training. Finally, the CWNN gives its own interpretations of multitemporal SAR images and generates a final change map. It is challenging to apply CWNN to change detection, since the number of training samples is limited. In order to solve this problem, a virtual samples' generation method is employed to create samples from the imaging procedure perspective.

The main contributions of this letter are twofold. First, we introduce dual-tree complex wavelet transform (DT-CWT) into sea ice change detection from SAR images to reduce the effect of speckle noise. The CWNN can exploit change information from multitemporal images and effectively improves the change detection performance. Second, to address the problem of limited training samples, a virtual samples' generation method is utilized to create samples. We employed the proposed method on two real SAR data sets, and the proposed method achieved excellent performances, especially in noisy backgrounds.

II. Methodology

A. Problem Statements and Overview of the Proposed Method

Let us consider two coregistered SAR images I_1 and I_2, which are acquired over the same polar region at different times t_1 and t_2. The purpose of sea ice change detection is aiming at producing a difference image that represents the change information between t_1 and t_2. The general framework of the proposed method is shown in Fig. 1. The proposed method is mainly composed of three steps.

Step 1 (Preclassification): The log-ratio operator is used to generate the difference image I_D. Then, the fuzzy c-means (FCM) algorithm is employed to classify the difference image into three clusters.

Step 2 (Sample Image Patches' Generation): Image patches around each pixel are generated. Patches with high probability to be changed or unchanged are taken as training samples, and some virtual sample patches are also generated.

Step 3 (Classification by CWNN): The image patches generated in Step 2 are treated as training data and fed into the CWNN. After training, all sample patches from the original multitemporal SAR images are fed into the learned CWNN for classification, and then, the final change map can be obtained.

Section II is organized as follows. The descriptions of preclassification and sample image patches generation algorithms are provided in Section II-B. Section II-C gives the detailed descriptions of CWNN.

B. Preclassification and Sample Image Patches' Generation

The log-ratio operator is first used to convert the linear scale of SAR image to a logarithmic scale before a change information analysis. The log-ratio image I_D is computed by $I_D = |\log(I_2/I_1)|$. It is well acknowledged that the multiplicative noise can be transformed to additive noise by the log-ratio operator. After obtaining I_D, a hierarchical FCM algorithm is performed on I_D to classify pixels into three groups: the changed class Ω_c, the unchanged class Ω_u, and the intermediate class Ω_i. Pixels belonging to Ω_c have a high probability of being changed, and pixels belonging to Ω_u have a high probability to be unchanged. Thus, Ω_c and Ω_u are selected as training samples. Pixels belonging to Ω_i will be further classified by CWNN. The detailed description of the hierarchical FCM algorithm can be found in [2].

Image patches centered at pixels belonging to Ω_c and Ω_u are extracted from the original SAR images. Let $P_k^{I_1}$ represent a patch centered at pixel k in image I_1 and $P_k^{I_2}$ represent the corresponding patch in image I_2. The size of each patch is $w \times w$. Both the patches are concatenated into a new image patch P_k, and the size of P_k is $2w \times w$. Let N represent the number of pixels belonging to Ω_c and Ω_u; therefore, we obtain the sample images $\{P_k\}, k = 1, 2, \ldots, N$. Features of these samples will be extracted and trained by CWNN.

In fact, there are many weights need to be tuned in CWNN. Therefore, inappropriate weights may cause the training process getting trapped in a local minimum of the loss function, and these weights would incur poor performance in change detection [18]. To obtain good weights, large quantities of samples are needed in the training process. However, in SAR image change detections, the number of available samples is limited. To solve the problem, we generate virtual samples for the purpose of enriching the training samples.

A virtual sample P_k' can be generated from two given samples of the same class with proper ratios

$$P_k' = \alpha P_i + (1-\alpha) P_j + \beta \tag{1}$$

where P_i and P_j are two training samples from the same class. Here, α is uniformly distributed random value on the interval [0, 1]. β denotes the random Gaussian noise. The mean of β is set to 0, and the variance of β is set to 0.001. A similar virtual sample generation method was employed in the hyperspectral image classification in Chen *et al.*'s work [18]. It is demonstrated that under the condition of limited training samples, the classification model with virtual samples outperformed the model without virtual samples. Considering that a virtual sample generated by two samples of the same class still belongs to the same class, we assign the same label of training samples to the virtual sample P_k'. We randomly generate N samples from the real samples $\{P_k\}, k = 1, 2, \ldots, N$. Then,

the real samples and virtual samples are used together as training samples to obtain proper weights in the CWNN.

C. Classification by Convolutional-Wavelet Neural Networks

The aim of CWNN is to learn the discriminative features, and these features can distinguish the changed information from multitemporal SAR images. CWNN is derived from CNN, which is consisted of various combinations of convolutional layers, max-pooling layers, and fully connected layers. At the beginning layer, CNN extracts elementary visual features, such as oriented edges, endpoints, and corners. These features are combined by the subsequent layers to form high-level features. However, the intrinsic speckle noise in SAR images will affect the classification performance. The max pooling in CNN is considered to have lost some basic structures (such as edges, endpoints, and corners). Therefore, it is important to preserve more basic structures at the pooling layer.

To tackle the above-mentioned problem, CWNN [15] introduced DT-CWT into CNN to reduce the effect of speckle noise. DT-CWT is considered to have a good performance in directional selectivity, limited redundancy, and perfect reconstruction. Thus, the layer preceding the pooling layer can be decomposed into eight components by DT-CWT. The eight components include two low-frequency subbands LL_1 and LL_2 and the high-frequency subbands in six orientations, $\pm 15°$, $\pm 45°$, and $\pm 75°$ (represented by LH_1, LH_2, HL_1, HL_2, HH_1, and HH_2). The average of the two low-frequency subbands is selected as the output of the pooling layer.

There are two advantages by introducing DT-CWT into CNN. First, low-frequency subbands keep the structures of input layer according to the specified rules, which lead to a better representation of the input. Second, by losing the high-frequency subbands, some speckle noises can be effectively suppressed. In our implementation, the input of a wavelet pooling layer is the output of the previous convolutional layer. For each input feature map x, we use DT-CWT to obtain the subbands

$$\{\mathrm{LL}_1, \mathrm{LL}_2, \mathrm{LH}_1, \mathrm{LH}_2, \mathrm{HL}_1, \mathrm{HL}_2, \mathrm{HH}_1, \mathrm{HH}_2\} = f(x_i) \quad (2)$$

where the DT-CWT function $f(\cdot)$ generates the eight components. Then, the average of the low-frequency subbands is used as the output of the wavelet pooling layer, which is defined as

$$\mathrm{LL}_{\mathrm{mean}} = \frac{1}{2}(\mathrm{LL}_1 + \mathrm{LL}_2) \quad (3)$$

where $\mathrm{LL}_{\mathrm{mean}}$ is the output of the wavelet pooling layer.

The architecture of CWNN is shown in Fig. 2. The two convolutional layer is expressed as C_2 and C_4, and the wavelet pooling layer is expressed as W_3 and W_5. Therefore, the network can be expressed as $\{I_1, C_2, W_3, C_4, W_5, F_6, O_7\}$. I_1 is the input layer, and all the input image patches are resampled to the size of 28×14. C_2 is a convolutional layer with six convolutional kernels whose sizes are 5×3. This layer produces six feature maps with the size of 24×12. W_3 is a wavelet pooling layer. In this layer, all the input feature maps are decomposed with one-level DT-CWT. This wavelet pooling layer produces six feature maps with the size of 12×6. C_4 is a convolutional layer with 12 convolutional kernels whose sizes are 5×3. This layer generates 12 feature maps with the size of 8×4. W_5 is a wavelet pooling layer, and it produces 12 feature maps with the size of 4×2. F_6 is the fully connected layer with 96 units. O_7 is the output layer with two units. The two units represent the changed and unchanged classes, respectively.

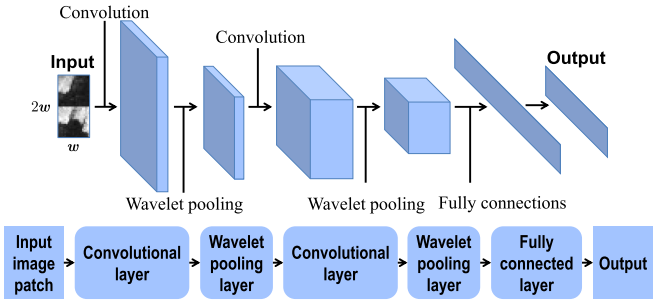

Fig. 2. Network architecture of CWNN.

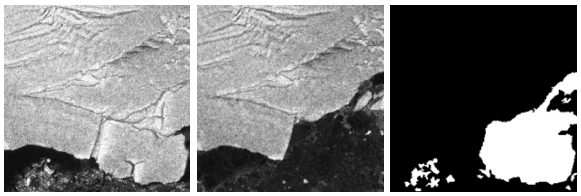

Fig. 3. Illustration of the data set I. (a) Image acquired in March 11, 2011. (b) Image acquired in March 16, 2011. (c) Ground truth.

As mentioned earlier, the real samples and virtual samples are combined together as training samples for CWNN training. After training, image patches from Ω_i are further classified into changed and unchanged classes. Finally, we combine the CWNN classification result and the preclassification result together to form the final change map.

III. Experimental Results and Analysis

A. Experimental Setup

The proposed method is evaluated quantitatively and qualitatively on two data sets. Both the data sets are acquired from two large SAR images of the region of the Sulzberger Ice Shelf. The two SAR images are acquired by the European Space Agency's Envisat satellite on March 11 and 16, 2011. Both the images show the progression of the ice breakup. When the Tohoku Tsunami was triggered in the Pacific Ocean on March 11, 2011, massive ocean waves caused the ice shelf to flex and break. The original size of both the SAR images is 2263×2264 pixels. They are too huge to show the detailed information, and therefore, we select two typical areas (256×256 pixels for each area). Both the data sets and the available ground-truth images, which are obtained by integrating prior information with photointerpretation, are shown in Figs. 3 and 4, respectively.

The performance evaluation of change detection is an important issue. We use false positives (FPs), false negatives (FNs), overall error (OE), percentage correct classification (PCC), and Kappa coefficient (KC) as the indicators to measure the effectiveness of the proposed method. The FP is

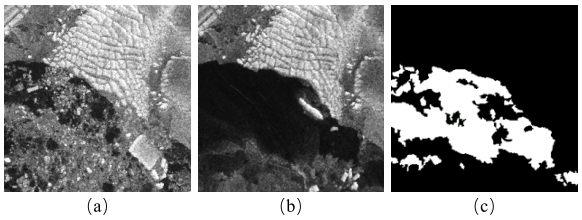

Fig. 4. Illustration of the data set II. (a) Image acquired on March 11, 2011. (b) Image acquired on March 16, 2011. (c) Ground truth.

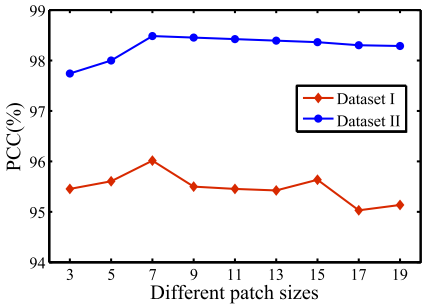

Fig. 5. Change detection results versus different patch sizes on both data sets.

the number of pixels that are unchanged pixels in the ground-truth image but wrongly classified as changed ones. The FN is the number of pixels that are changed class in the ground-truth image but wrongly classified as unchanged ones. The OE is computed by OE = FP + FN. The PCC is computed by PCC = $(Nt - \text{OE})/Nt \times 100\%$, where Nt represents the total pixels in the ground-truth image. The KC gives the percentage of agreement (correct classified pixels) corrected by the number of agreements that would be expected by chance. The detailed information about KC can be found in [16].

In order to demonstrate the effectiveness of the proposed sea ice change detection method, four closely related methods were implemented for comparison purpose: NBRELM [2], PCAKM [6], GaborPCANet [17], and CNN. These methods are implemented using the authors' publicly available source codes. In our implementations, we randomly select 10 000 pixels from Ω_u and Ω_c as real samples. It should be noted that the positive and negative samples are equally distributed, which means that 50% samples are selected from Ω_c, while 50% samples are selected from Ω_u. Then, we generate 10 000 virtual samples based upon these real samples.

The patch size w is an important parameter. As shown in Fig. 5, if w is too large ($w \geq 9$), the change detection result tends to get worse, since the patch is not representative for the specified position. If w is too small ($w \leq 5$), it will be detrimental to denoising. Therefore, we set $w = 7$ in our implementations.

B. Results and Analysis

We first test the effectiveness of virtual samples. As listed in Table I, by using virtual samples in classification, the PCC values are improved by 0.07% and 0.20% on the data sets I and II, respectively. The KC values are also improved by using virtual samples. This proves that the CWNN with virtual samples is an efficient tool for sea ice change detection.

TABLE I
CHANGE DETECTION RESULTS OF CWNN AND CWNN WITH VIRTUAL SAMPLES

Methods	Dataset I		Dataset II	
	PCC(%)	KC(%)	PCC(%)	KC(%)
CWNN	98.41	94.92	96.01	89.73
CWNN with virtual samples	98.48	95.17	96.21	90.23

TABLE II
CHANGE DETECTION RESULTS OF DIFFERENT METHODS ON DATA SET I

Methods	FP	FN	OE	PCC(%)	KC(%)
NBRELM [2]	817	673	1490	97.73	92.76
PCAKM [6]	711	479	1190	98.18	94.23
GaborPCANet [17]	473	739	1212	98.15	94.04
CNN	796	364	1160	98.23	94.41
Proposed method	574	419	993	98.48	95.17

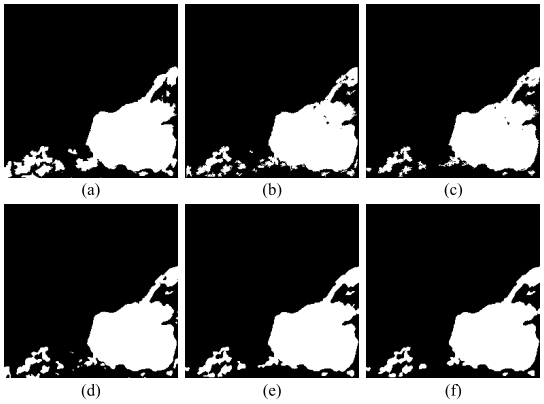

Fig. 6. Visualized results of various change detection methods on data set I. (a) Ground truth. (b) Result by NBRELM [2]. (c) Result by PCAKM [6]. (d) Result by GaborPCANet [17]. (e) Result by CNN. (f) Result by the proposed method.

The final change detection change maps are shown in the figure form and the evaluation criteria are shown in the tabular form. The results of the experiments on both the data sets are listed in Figs. 6 and 7, respectively.

Table II lists the quantitative evaluation results on data set I, from which it can be concluded that the proposed method performs better than the other methods. Furthermore, from Fig. 6, it can be observed that there are many small noisy regions in the change maps generated by PCAKM and GaborPCANet. Therefore, the FP values of PCAKM and GaborPCANet are relatively high. High FP values affect the overall performance of both the methods. The PCC value of the proposed method on this data set is improved by 0.75%, 0.30%, 0.33%, and 0.15% over NBRELM, PCAKM, GaborPCANet, and CNN, respectively. At the same time, the KC value of the proposed method is improved by 2.41%, 0.94%, 1.13% and 0.67% over NBRELM, PCAKM, GaborPCANet, and CNN, respectively. It is well worth noting that KC is the most persuasive coefficient in change detection tasks. Thus, we draw the conclusion that the proposed method outperforms the other methods on this data set.

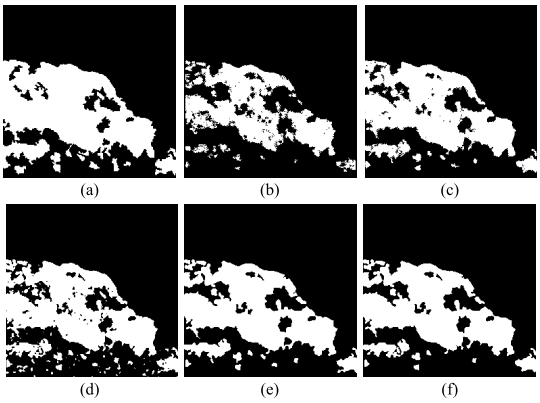

Fig. 7. Visualized results of various change detection methods on data set II. (a) Ground truth. (b) Result by NBRELM [2]. (c) Result by PCAKM [6]. (d) Result by GaborPCANet [17]. (e) Result by CNN. (f) Result by the proposed method.

TABLE III
CHANGE DETECTION RESULTS OF DIFFERENT METHODS ON DATA SET II

Methods	FP	FN	OE	PCC(%)	KC(%)
NBRELM [2]	539	2782	3321	94.93	85.82
PCAKM [6]	3073	362	3435	94.76	86.74
GaborPCANet [17]	2475	500	2975	95.46	88.35
CNN	2576	306	2882	95.60	88.78
Proposed method	2120	365	2485	96.21	90.23

Table III lists the quantitative evaluations results on data set II, from which it can be observed that the PCC and KC values of the proposed method are obviously better than the other methods. In this data set, there are many noisy regions. From Fig. 7, we can observe that many unchanged pixels are falsely classified into the changed class by PCAKM and GaborPCANet. Hence, the FP values of both the methods are relatively high in Table III, which affects the overall change detection performance of both the methods. The proposed method can exploit effective feature representations from the multitemporal SAR images, and the KC value of the proposed method is improved by 4.41%, 3.49%, and 1.88% over NBRELM, PCAKM, and GaborPCANet, respectively. Furthermore, the proposed method outperforms the CNN in terms of PCC and KC, which proves that the CWNN with wavelet pooling and virtual sample is a powerful tool for SAR image change detection. Therefore, we can draw the conclusion that the proposed method outperforms the other methods on this data set. The visual and quantitative analyses on both the data sets demonstrate the effectiveness of the proposed method.

IV. CONCLUSION

This letter has presented a sea ice change detection method for SAR image-based CWNN. Wavelet transform is introduced into sea ice change detection to reduce the effect of speckle noise from SAR images. The CWNN can effectively exploit change information from multitemporal images. In addition, a virtual samples' generation method is utilized to create samples, and the problem of limited training samples is alleviated. The robustness and reliability of the proposed method are evaluated using Envisat images. The experimental results confirmed that the proposed method can achieve a better performance than four closely related methods.

REFERENCES

[1] L. Wang, K. A. Scott, L. Xu, and D. A. Clausi, "Sea ice concentration estimation during melt from dual-pol SAR scenes using deep convolutional neural networks: A case study," *IEEE Trans. Geosci. Remote Sens.*, vol. 54, no. 8, pp. 4524–4533, Aug. 2016.

[2] F. Gao, J. Dong, B. Li, Q. Xu, and C. Xie, "Change detection from synthetic aperture radar images based on neighborhood-based ratio and extreme learning machine," *J. Appl. Remote Sens.*, vol. 10, no. 4, Dec. 2016, Art. no. 084684.

[3] M. Gong, H. Yang, and P. Zhang, "Feature learning and change feature classification based on deep learning for ternary change detection in SAR images," *J. Photogramm. Remote Sens.*, vol. 129, pp. 212–225, Jul. 2017.

[4] Y. Bazi, L. Bruzzone, and F. Melgani, "Automatic identification of the number and values of decision thresholds in the log-ratio image for change detection in SAR images," *IEEE Geosci. Remote Sens. Lett.*, vol. 3, no. 3, pp. 349–353, Jul. 2006.

[5] Y. Bazi, F. Melgani, and L. Bruzzone, "A genetic expectation-maximization method for unsupervised change detection in multitemporal SAR imagery," *Int. J. Remote Sens.*, vol. 30, no. 24, pp. 6591–6610, Dec. 2009.

[6] T. Celik, "Unsupervised change detection in satellite images using principal component analysis and k-means clustering," *IEEE Geosci. Remote Sens. Lett.*, vol. 6, no. 4, pp. 772–776, Oct. 2009.

[7] M. Gong, Z. Zhou, and J. Ma, "Change detection in synthetic aperture radar images based on image fusion and fuzzy clustering," *IEEE Trans. Image Process.*, vol. 21, no. 4, pp. 2141–2151, Apr. 2012.

[8] H.-C. Li, T. Celik, N. Longbotham, and W. J. Emery, "Gabor feature based unsupervised change detection of multitemporal SAR images based on two-level clustering," *IEEE Geosci. Remote Sens. Lett.*, vol. 12, no. 12, pp. 2458–2462, Dec. 2015.

[9] Q. Wang, Z. Meng, and X. Li, "Locality adaptive discriminant analysis for spectral–spatial classification of hyperspectral images," *IEEE Geosci. Remote Sens. Lett.*, vol. 14, no. 11, pp. 2077–2081, Nov. 2017.

[10] Q. Wang, J. Wan, and Y. Yuan, "Deep metric learning for crowdedness regression," *IEEE Trans. Circuits Syst. Video Technol.*, vol. 28, no. 10, pp. 2633–2643, Oct. 2018, doi: 10.1109/TCSVT.2017.2703920.

[11] Q. Wang, J. Gao, and Y. Yuan, "A joint convolutional neural networks and context transfer for street scenes labeling," *IEEE Trans. Intell. Transp. Syst.*, vol. 19, no. 5, pp. 1457–1470, May 2018.

[12] Q. Wang, J. Gao, and Y. Yuan, "Embedding structured contour and location prior in siamesed fully convolutional networks for road detection," *IEEE Trans. Intell. Transp. Syst.*, vol. 19, no. 1, pp. 230–241, Jan. 2018.

[13] Q. Wang, Z. Yuan, Q. Du, and X. Li, "GETNET: A general end-to-end 2-D CNN framework for hyperspectral image change detection," *IEEE Trans. Geosci. Remote Sens.*, vol. 57, no. 1, pp. 3–13, Jan. 2019, doi: 10.1109/TGRS.2018.2849692.

[14] B. Pan, Z. Shi, and X. Xu, "R-VCANet: A new deep-learning-based hyperspectral image classification method," *IEEE J. Sel. Topics Appl. Earth Obser. Remote Sens.*, vol. 10, no. 5, pp. 1975–1986, May 2017.

[15] Y. Duan, F. Liu, L. Jiao, P. Zhao, and L. Zhang, "SAR image segmentation based on convolutional-wavelet neural network and Markov random field," *Pattern Recognit.*, vol. 64, pp. 255–267, Apr. 2017.

[16] R. L. Brennan and D. J. Prediger, "Coefficient kappa: Some uses, misuses, and alternatives," *Edu. Psychol. Meas.*, vol. 41, no. 3, pp. 687–699, Oct. 1981.

[17] F. Gao, J. Dong, B. Li, and Q. Xu, "Automatic change detection in synthetic aperture radar images based on PCANet," *IEEE Geosci. Remote Sens. Lett.*, vol. 13, no. 12, pp. 1792–1796, Dec. 2016.

[18] Y. Chen, H. Jiang, C. Li, X. Jia, and P. Ghamisi, "Deep feature extraction and classification of hyperspectral images based on convolutional neural networks," *IEEE Trans. Geosci. Remote Sens.*, vol. 54, no. 10, pp. 6232–6251, Oct. 2016.